

Infrared Emission (500-2000 cm^{-1}) of Laboratory Ice Clouds

Carl G. Schmitt, and W. Patrick Arnott*

Desert Research Institute

Reno NV 89506

Corresponding author, email address pat@dri.edu.

ABSTRACT

The spectral infrared emission (500-2000 cm^{-1}) of laboratory ice clouds has been measured with a fourier transform infrared spectrometer. A cloudscope (a novel microscope equipped with a video camera) captured cloud ice crystals for microphysical characterization of the cloud. Theoretical emission calculations based on modified Mie theory, observed crystal size distributions, and an approximation for IR radiative transfer agree reasonably well with measurements. Model sensitivity to anomalous diffraction theory, size distribution, and particle shape are explored. Atmospheric applications are that the single scattering approximation is dubious; that the zero scattering approximation is accurate to within 20% in the atmospheric window region; and that recent observations of strong spectral variations in the upwelling IR emission from some cirrus is largely due to contributions by small ice crystals. The ratio of visible optical depth to IR optical depth at 10.85 μm (the "LIRAD" ratio) was 2.4, and is at the lower end of reported values from tropical cirrus despite the relatively small laboratory crystal sizes observed.

1. INTRODUCTION

Young contrails and high altitude tropical cirrus clouds generally contain ice crystals with maximum dimensions less than 50 μm .¹⁻³ Cirrus containing these small ice crystals can have important radiative influences on climate.⁴ It has been shown that cirrus composed mainly of small ice crystals can have both a positive or negative net cloud radiative forcing (loosely, a warming or cooling effect on the Earth's surface temperature), depending on the cirrus cloud cover that can be quantified using the ice water path (IWP).^{5,6} The abrupt change from the usual warming influence of cirrus on surface temperature to a cooling effect occurred over a narrow range of IWP. Cirrus with small effective diameters and small IWP have a warming influence on climate,^{4,5} though as the IWP increases the solar albedo increases sufficiently to offset the warming effect in the IR so that the net radiative forcing of cirrus can be a cooling effect on climate. Cirrus with larger effective diameter crystals generally has a net warming influence.⁵ The cold temperatures and associated lack of moisture of the high altitude tropical cirrus results in small crystal sizes and concentrations, and could be very important for maintenance of the tropical ocean warm pool temperature.⁴

Radiative observations of a thin cirrus layer have been made by a downward looking infrared spectrometer and a visible wavelength lidar.⁷ The layer had a strong IR spectral signature indicating both the presence of small ice crystals, and a strong extinction; yet the lidar signal was weak. Similar spectral variation has been previously observed in satellite IR emission measurements over the ocean where thin cirrus was present.^{4,8} In these measurements land or ocean surfaces are warm IR emitters, and the zeroth order influence of the thin cirrus is to attenuate this emission before it reaches the satellite or aircraft sensor. The spectral signature is related to the spectral extinction by small ice crystals.⁹

Prediction of the longwave component of small ice crystal climatic impact depends on knowledge of the infrared radiative properties. Laboratory measurements are useful for understanding and simulating these properties in a controlled environment where crystals can be well characterized. Such measurements are also useful in evaluation of new exact and approximate computational methods for obtaining single scattering cross sections,¹⁰ and for radiative transfer theory development. This paper describes laboratory ice cloud infrared emission spectra and compares these results with theory. Section 2 is the theory of cloud emission and section 3 describes the experimental arrangement. Section 4 displays the laboratory cloud IR emission measurements, and compares the results to theory. Section 5 considers atmospheric applications.

2. CLOUD EMISSION THEORY

A theoretical model for cloud infrared emission was adapted from the theory for remotely sensing stack emissions,¹¹ though the extension to include multiply scattered emission was necessary. A summary of the model is given below. A simplified diagram of the laboratory emission set-up is shown in Fig. 1. The emission from the blackbody opposite the Fourier transform infrared spectrometer (FTIR) will be attenuated by the cloud before reaching the FTIR.

The radiance is given by

$$I_{bb} = B(T_{bb}, \nu) \exp[-\beta_{ext}(\nu)L]. \quad (1)$$

In Eq. (1), $B(T_{bb}, \nu)$ is the radiance from a blackbody of temperature T_{bb} at wavenumber ν , L is the cloud length, and $\beta_{ext}(\nu)$ is the cloud extinction coefficient (gas and particle).

An element of cloud having thickness dz has emission dI_c that is also attenuated by the remainder of the cloud that rests between dz and the spectrometer. The cloud emission in dz is

$$dI_c^{(0)} = B(T_c, \nu) \{ \beta_{abs}(\nu) dz \} \exp[-\beta_{ext}(\nu)(L-z)]. \quad (2)$$

In this expression, T_c is the cloud temperature, $\beta_{abs}(\nu)$ is the local cloud absorption coefficient (gas and particle) in dimensions of inverse distance, and z is the location of the cloud slab dz . The combination of the first two terms is the gray body emission by the cloud slab, and the next term is the attenuation in the cloud between the slab and the spectrometer. Taking the limit as dz gets very small, and integrating Eq. (2) over the entire cloud length L gives the radiance due to cloud emission and extinction in the direct view of the spectrometer,

$$I_c^{(0)}(\nu, L) = B(T_c, \nu) \left[\frac{\beta_{abs}(\nu)}{\beta_{ext}(\nu)} \right] [1 - \exp(-\beta_{ext}(\nu)L)] \quad (3)$$

This relation already includes one consequence of IR scattering by particles in the component of extinction due to scattering. However, it does not include the cloud radiance from outside the view of the spectrometer that is scattered by the cloud slab into the field of view. The cloud emission from outside the field of view that is then scattered by the cloud slab dz into the field of view is

$$dI_c^{(1)} = I_c^{(0)}(\nu, L_w) \{ \beta_{sca}(\nu) dz \} \exp[-\beta_{ext}(\nu)(L-z)]. \quad (4)$$

In this expression, $\beta_{sca}(\nu)$ is the local cloud scattering coefficient (particle only, Rayleigh scattering by gases is negligible in the infrared) in dimensions of inverse distance, and L_w is the distance from the cloud element to the chamber wall. In this expression, the zeroth order radiance is from cloud outside the spectrometer field of view, and is taken to be incident on the particle in the cloud slab uniformly from all directions (thus the approximate use of the total scattering cross section in Eq. (4)). The total emission that is scattered only once by the cloud slab is obtained by integration of Eq. (4) as

$$I_c^{(1)}(\nu, L) = I_c^{(0)}(\nu, L_w) \left[\frac{\beta_{sca}(\nu)}{\beta_{ext}(\nu)} \right] [1 - \exp(-\beta_{ext}(\nu)L)] \quad (5)$$

This process can be repeated to obtain the contribution of emission from outside the field of view that is scattered once (or multiple times) from outside the field of view before finally being scattered by the cloud slab to the spectrometer. Expressing the total cloud radiance scattered and emitted as a sum, and recognizing that the sum is a simple geometric series, the result is

$$I_c(\nu) = B(T_c, \nu) \left[\frac{\beta_{abs}(\nu)}{\beta_{abs}(\nu) + \beta_{sca}(\nu) \exp(-\beta_{ext}(\nu)L_w)} \right] [1 - \exp(-\beta_{ext}(\nu)L)] \quad (6)$$

In the numerical implementation of the theory, the distance between the cloud and the wall is taken to be $L_w = L$ since L is a characteristic length of the chamber. Cloud radiance vanishes as absorption goes to zero, and for very large optical depth and non-zero absorption coefficient, cloud radiance reduces to blackbody radiance at the cloud temperature.

The IR radiation from the walls is similarly scattered by particles into the field of view, and is approximated by a procedure similar to that leading up to Eq. (4);

$$I_w(\nu) = B(T_w, \nu) \exp(-\beta_{ext}(\nu)L_w) \frac{\beta_{sca}(\nu)}{\beta_{ext}(\nu)} [1 - \exp(-\beta_{ext}(\nu)L)] \quad (7)$$

where T_w is the wall temperature (taken to be the cloud temperature T_c in the numerical implementation), and the wall is assumed a blackbody. Note that wall radiance contribution vanishes when particle scattering goes to zero, when the cloud optical depth is so large that wall radiance is strongly attenuated, and that absorption (by particles and gases) only reduces the contribution of wall radiance scattered by particles. This scattering model is only approximate in that the exact geometry of the scattering chamber is not accounted for, nor is the fact that blackbody T_{bb} is the source of IR on the main field of view of the spectrometer, nor is the departure from unity of emissivity of the frost covered walls. A more sophisticated model would consider the differential scattering cross section for particles, and would integrate the IR radiation from each wall element. While this wall correction is approximate, it supplies a

necessary spectral contribution where scattering by particles is strong (where the real part of the refractive index deviates significantly from unity).

The total emission exiting the chamber is

$$I(\nu) = I_{bb}(\nu) + I_w(\nu) + I_c(\nu). \quad (8)$$

I_{bb} is the attenuated emission from the blackbody behind the cloud. I_w is the IR from the walls scattered by the cloud. I_c is the emission from the cloud. If the blackbody behind the cloud is cold enough that it has negligible emission, the first term can be ignored, and the cloud emission and scattering dominate. Gaseous emission and extinction from the chamber to the spectrometer modify this radiance. The radiance received at the spectrometer is given by

$$I_{spec}(\nu) = I(\nu) \exp(-\beta_{abs,g}(\nu)L_{spec}) + B(T_r) \left[1 - \exp(-\beta_{abs,g}(\nu)L_{spec}) \right], \quad (9)$$

where $\beta_{abs,g}(\nu)$ is the absorption coefficient of water vapor and carbon dioxide at room temperature T_r , and L_{spec} is the distance between the chamber opening and the spectrometer. The room temperature gaseous absorption and emission was confined to well defined spectral intervals, leaving the emission in the spectral interval between 750 cm^{-1} and 1250 cm^{-1} due almost entirely to particles.

2.2 Ice crystal geometry, size distribution model, and approximate radiative cross sections

The assumed ice crystal geometry is simple hexagonal plates and columns. This assumption is reasonable for the laboratory ice clouds, but many or most cirrus clouds contain crystals that deviate from this simple shape. Let D and H represent the diameter of the circle that just touches the hexagonal perimeter and the crystal height parallel to the c axis. The average projected area P of a randomly oriented crystal, and the crystal volume V , are given by

$$P = \frac{3}{4} DH + \frac{3\sqrt{3}}{16} D^2, \quad (10)$$

and

$$V = \frac{3\sqrt{3}}{8} D^2 H . \quad (11)$$

A sphere diameter, D_s , was chosen based on conserving the ratio V/P , and is given by

$$D_s = \frac{3V}{2P} . \quad (12)$$

The ice crystal cross sections for absorption, scattering, and extinction were estimated from

$$\sigma(v, D, H) = P(D, H) Q[v, D_s(D, H)] , \quad (13)$$

where σ is a radiative cross section, and Q is a dimensionless efficiency factor computed from

either Mie or anomalous diffraction theories. This method of computing the absorption cross

section is asymptotically matched at the small particle limit where Q is proportional to V/P and

σ is proportional to V , and is matched at the large particle limit where σ is proportional to P

and Q approaches a constant value near 1 or 2 for absorption and extinction,

respectively.^{12,13,14} However, as we will show, the choice of theory to use for computing Q

has a relatively strong influence on the agreement with measurements. Integration of these cross

sections over size distributions reduces the strong size dependent behavior of Mie theory for

spheres.

The aspect ratios for plate and column crystals are from the relations

$$H(D) = 0.737 D^{0.6885} , \quad (14)$$

where D and H are in μm units, and

$$D(H) = 0.666 H . \quad (15)$$

These empirical relations were obtained from measurements during the course of the experiments, as discussed in Section 3.

The gamma function size distribution model has 3 parameters, and is given by

$$n(D) = \frac{N D^{x-1} \exp(-D/D_0)}{\Gamma(x) D_0^x} \quad (16)$$

where $n(D)$ is the concentration per size interval; $\Gamma(x)$ is the gamma function; N is the total concentration;

$$x = 4 \left(\frac{\langle D \rangle}{W} \right)^2; \quad (17)$$

W is the width of the distribution; $\langle D \rangle$ is the mean diameter of the distribution; and $D_0 = \langle D \rangle/x$. The mean diameter and distribution width needed in Eq. (16) are obtained from the measured size distribution $n_m(D_i)$ with bins of width ΔD_i and midpoints D_i using the following relations:

$$\langle D \rangle = \frac{\sum_i n_m(D_i) D_i \Delta D_i}{\sum_i n_m(D_i) \Delta D_i}, \quad (18)$$

and

$$W = 2 \sqrt{\frac{\sum_i n_m(D_i) (D_i - \langle D \rangle)^2 \Delta D_i}{\sum_i n_m(D_i) \Delta D_i}}. \quad (19)$$

The total concentration N is determined from the measured optical depth through the relation

$$N = \frac{\tau_{685nm}}{\sum_j n(D_j; N=1) \sigma_{ext}(D_{sj}, 685nm) \Delta D_j L}, \quad (20)$$

where τ_{685nm} is the measured optical depth using the 685 nm wavelength laser diode; $n(D_j; N=1)$

is the gamma distribution from Eq. (16) evaluated for $N=1$; ΔD_j is the bin width of the

discretized size distribution where bin mid-points are given by D_j ; $\sigma_{ext}(D_{sj}, 685 \text{ nm})$ is the Mie

theoretic extinction cross section for a wavelength of 685 nm; and L is the cloud length.

(NOTE: $\sigma_{ext}(D_{sj}, 685 \text{ nm})$ is actually computed using linear interpolation given in Eq. (21)).

The gamma size distribution was discretized to cover a size range from 0.5 μm to 100.5 μm with a spacing of $\Delta D_j = 1 \mu\text{m}$ between points. The radiative coefficients needed to arrive at the computed emission in Eq. (9) are obtained from

$$\beta(\nu) = \sum_j n(D_j) P(D_j, H_j) \left[Q(\nu, D_{sj}^{(1)}) + \left\{ Q(\nu, D_{sj}^{(2)}) - Q(\nu, D_{sj}^{(1)}) \frac{D_{sj} - D_{sj}^{(1)}}{D_{sj}^{(2)} - D_{sj}^{(1)}} \right\} \right] \Delta D_j, \quad (21)$$

where the linear interpolation of efficiency factors is needed because the equivalent sphere diameters D_{sj} generally are not one of the integer values $D_j = 1, 2, \dots, 100 \mu\text{m}$. In this expression, $D_{sj}^{(1)} = \text{INT}(D_{sj})$ and $D_{sj}^{(2)} = D_{sj}^{(1)} + 1 \mu\text{m}$, where the function INT obtains the integer portion of the real number by cleaving off the fractional part. The theoretical matrices $Q(D_{sj}, \nu)$ formed by values of wavenumber and particle size were computed once and used many times (in fact, for speed and compactness, it was compiled directly into the final program as a very large data statement). The refractive index of ice was from Warren. ¹⁵

Gaseous absorption coefficients for water vapor and carbon dioxide were computed at a spectral resolution of 0.0034 cm^{-1} , to ensure that the individual lines are sufficiently resolved, using the commercial line by line code (HITRANPC available from ONTAR Corp.) that implements the hitran 96 spectral cross sections data base. The gaseous spectra calculations were performed once for a temperature of -15 C and a fiducial concentration. Then the actual gas concentrations computed using 360 ppm CO_2 , a water vapor $\text{RH} = 100\%$ in the chamber, and a $\text{RH} = 20\%$ in the room were used to properly scale these coefficients. Particle cross sections were interpolated to this resolution (reasonable because they vary slowly with ν). To make comparisons with the observed spectra, the results of this high resolution calculation were

averaged using a triangular window function to the spectral resolution of the spectrometer during most measurements, 4 cm^{-1} . The triangular window function $\text{WN}(v; v_c, \Delta v)$ is given by

$$\text{WN}(v; v_c, \Delta v) = 1 - \frac{|v - v_c|}{\Delta v}, \quad (v_c - \Delta v) \leq v \leq (v_c + \Delta v), \quad (22)$$

where v_c is the wavenumber where the emission is desired, and Δv is the desired spectral resolution. The spectrally averaged emission spectra $I_{spec}(v_c)$ is obtained from

$$I_{spec}(v_c) = \frac{\sum_k \text{WN}(v_k; v_c, \Delta v) I_{spec}(v_k)}{\sum_k \text{WN}(v_k; v_c, \Delta v)}, \quad (23)$$

and is compared with measurements in Section 4.

3. CLOUD EMISSION MEASUREMENTS

This section describes the experimental configuration to measure spectral infrared emission by laboratory ice clouds. Section 3.1 describes the methods used for the FTIR emission measurements. Section 3.2 describes the experimental ice cloud growth chamber. Section 3.3 describes the particle observation system (i.e. the cloudscape.)

3.1 FTIR emission measurements

Two blackbodies of known emissivity and temperature are used to calibrate cloud radiance measurements. Two cone shaped blackbodies were used for these calibration measurements. The cones have a 5 cm diameter opening, and are 30 cm long (Fig. 2). The narrow cone angle ensures a large ray path for photons in the cone, and thus a near ideal blackbody emission source.¹⁶ The cones were constructed of 10 mil. brass covered with black paint. The outsides of the cones were immersed in either water or a water ethylene glycol and water mixture. Thermistor type temperature probes were used to obtain the liquid temperature,

which was assumed to be the cone temperature. One blackbody was filled with water and sealed, and was at ambient temperature. The other blackbody had a temperature-controlled ethylene glycol and water mixture circulated through it. Temperature control was achieved with a fluid circulation control unit.

The thermistor probe specifications indicated an accuracy of $\pm 0.2^{\circ}\text{C}$. For calibration purposes, the temperature of the hot blackbody source was taken to be 0.6°C less than the measured liquid temperature. The 0.6°C offset was determined by trial and error analysis of the emission of a liquid-nitrogen cooled blackbody (to be described next). The low radiance liquid nitrogen source originally indicated a small negative radiance, but use of the 0.6°C offset of the warm blackbody gave a small positive radiance and a reasonable brightness temperature. It is possible that the cone surface of the warm blackbody was at a lower temperature than the fluid due to connective heat transport by the air. Placing the warm blackbody in a vertical position with the opening facing downward minimized this convection.

A diagram of the emission mode setup for the FTIR is shown in Fig. 3. The spectrometer is a modified Bomem MB100 with both emission and transmission measurement capabilities and has been used previously for ice and water cloud extinction measurements. The FTIR emission port is facing an uncoated front surface gold mirror. The mirror can be rotated to point at either of the two calibration blackbodies, or the cloud chamber. The general experimental procedure was to take a cold blackbody measurement, followed by a hot blackbody measurement, then a measurement of the cloud chamber.

3.2 Laboratory cloud chamber

For the laboratory measurements, it was necessary to have a very low emission background to limit as much as reasonable the stray emission from the walls. A large cone shaped blackbody of similar cone angle to the calibration blackbodies was built for the purpose.

A cone made of 5-mil. brass was manufactured and attached to a brass rectangular box (Fig. 4). The interior was again coated with black paint. The box was filled with liquid nitrogen, which at a temperature of 77 K provided a suitably cold background. A thin film of frost typically formed on the interior of the cone after an hour. It was determined that this did not affect the radiative properties of the cone (frost is IR-black).

A 4.8 meter tall 30 cm diameter tube with a cooling system was mounted on the top of a 1m tall x 1.2m x 1.2m freezer (Fig. 5). Figure 6 shows a few typical temperature profiles for the chamber. Water droplets from an ultrasonic nebulizer were blown into the top of the tube. The droplets cooled as they slowly fell towards the bottom of the tube. Two meters from the top, the droplets encountered the cloud seeder (Fig. 7). The cloud seeder consisted of a spring that circulated through liquid nitrogen bath, and then into the chamber. The spring was cold enough to induce homogeneous nucleation of some ice crystals. Because of the difference in vapor pressure of ice versus water, water drops evaporate while the ice crystals grow. The crystals then descend into the lower chamber. The 3-m distance to the chamber was long enough that no water droplets were present in the lower chamber. With this setup, a continuous ice cloud could be maintained in the chamber for hours.

3.3 Ice crystal detection

A modified version of the cloudscope described previously⁹ was developed to observe cloud particles. This new cloudscope is shown schematically in Fig. 8. The cloudscope was redesigned to enhance the collection efficiency for small particles. To accomplish this, two things were changed. First, the surface for capturing the crystals was made much smaller. The collection surface is a 1-mm wide sapphire bar. A long working distance microscope objective was sufficiently far away from the sapphire so as not to impede the flow pattern at the contact

surface. The second improvement was in the velocity of the air stream as it went past the sapphire. A vacuum pump created a vacuum in four 5-gallon containers. A hose attached to the cloudscope was momentarily exposed to the vacuum to collect particles. The only way for air to get into the cloudscope was to go past the sapphire. The inlet was a 3-mm pipe. A flow meter gave an air velocity of approximately 3 m/s.

The collection efficiency of the cloudscope was difficult to determine because of its geometry. Rough estimates of the collection efficiency could be determined using results of previous analysis.¹⁷ Figure 9 shows the estimated collection efficiency of the cloudscope. Figure 10 shows some images of ice crystals obtained with the cloudscope.

The cloudscope sapphire and objective were heated to prevent ice build-up. Current flow through nickel chromium wire was computer-controlled to accomplish this. The computer was also used to monitor and recorded the chamber ambient temperature, the temperature of the microscope objective, the sapphire temperature, and the cloud visible optical depth. Optical depth was measured using a laser diode source at 685 nm, and a photodiode attached to an integrating sphere approximately 2 meters away from the cloud chamber to minimize the amount of forward scattering measured so that the this measurement was near ideal. Insufficient temperature differences between the sapphire or objective and the ambient cloud led to a voltage being applied to the heating resistors. The temperature differences could be adjusted manually on the computer to account for changing chamber conditions. It was necessary keep the sapphire temperature below freezing, otherwise crystals would melt on contact and habit information would be lost. Data was saved to a file and displayed on the computer monitor in graphical form in real time to provide an understanding of the overall system during measurements.

4. COMPARISON OF CLOUD EMISSION MEASUREMENTS AND THEORY

This section gives a description of the laboratory experiments. Section 4.1 describes the characteristics of the clouds that were grown in the laboratory. Section 4.2 is about the emission measurement taken of a cloudless chamber. Section 4.3 gives a description of the laboratory data. Section 4.4 describes several of the experimental results.

4.1 *Cloud characteristics*

The crystal geometry viewed with the cloudscope during the lab experiments is worth note. During one day of experiments, several of the plate-like crystals landed on edge then fell over (Fig. 11). Improved mass calculations were possible because both dimensions of the plate crystals were easily measured. Both dimensions of columnar crystals can be measured. The maximum dimension is plotted versus the thickness of the crystal, and a best-fit relation between the dimensions is given for both common types of crystals. Figure 12a shows the dimensions of the plate crystals that were observed and measured. Figure 12b shows the dimensions of column shaped crystals that were imaged. The curve fits were used in the numerical model.

4.2 *FTIR measurements of a cloudless chamber*

One side of the chamber had an 8-cm hole that the FTIR looked into. The wall on the opposite side of the chamber had a large hole, which was covered by the previously described liquid nitrogen cooled blackbody. A small amount of cloud was always present in the cold cone due to air being cooled to an extreme degree. Any water vapor would condense out upon being near the liquid nitrogen cooled surface. A small opening was left between the nitrogen-cooled blackbody and the chamber to allow for the unwanted cone cloud to fall out of the chamber and into the room rather than to pool in the bottom of the chamber. An emission measurement of the cloudless chamber is shown in Fig. 13.

Figure 13 clearly shows emission from carbon dioxide in the 625-725 cm^{-1} region. The small hump located in the 800 cm^{-1} region was due to the small amount of cloud present due to the liquid nitrogen cooled blackbody. The emission from this hump was small compared to cloud IR emission. The spectral features in the 1300-1800 cm^{-1} region are due to water vapor in the chamber and in the air between the chamber opening and the spectrometer.

4.3 Ice cloud emission data description

The emission from an ice cloud of plate crystals in the chamber is shown in Fig. 14a. This emission spectrum contains emission from the cloud as well as emission from the walls that was scattered by the cloud particles into the field of view of the spectrometer. A Christiansen band causes the slight dip near 1000 cm^{-1} . We found that this dip could only be accounted for when the chamber wall emission scattered by the cloud (see Eqs. (7) and (8)) was added to the total emission. In the wavenumber region of the dip, the cloud particles scatter comparatively less radiation because the real part of the ice refractive index is near unity.

The scattered emission depends on wavenumber, particle size, and particle geometry. Radiation scattered by a particle is dependent on the particle scattering cross section, and the incident radiative energy. The theoretical wall-scattered emission and the total emission including that from the cloud were obtained from the theory outlined in Sec. 2 and are shown in Fig. 14a. The upper panel shows the emissivity obtained by dividing the measured radiance spectra in the lower panel by the theoretical blackbody radiance for a temperature of -15 C. Note the slowly varying crystal cloud emission with superimposed rapidly varying contributions from CO_2 and H_2O gases.

The calculations in Fig. 14a, lower panel, were based on the cloudscope observed particle size distribution (Fig. 14b) once corrected for collection efficiency. Two particle size distributions are shown: the raw measured size distribution, and the collection efficiency

corrected (using the curve shown in Fig. 9) distribution. The mean diameter, measured visible optical depth, and the half-width of the observed distribution were calculated, and a theoretical smooth curve gamma distribution was created to match these quantities. The gamma distributions were used to calculate the theoretical IR spectra.

The sensitivity of radiance models to size distribution and theory are shown in Fig. 14c in the form of a difference between measurement and theoretical calculation. Note that the wavenumber range is just in the "atmospheric window" region where gaseous emission is less apparent. The curves labeled "Plates" and "Plates, Raw" were obtained using the modified Mie theory, the crystal geometry for plates (Fig. 12a), and the two gamma distributions shown in Fig. 14b. The sensitivity to size distribution is not dramatic, though it must be realized that the contributions to emission by particles of different sizes is weighted by particle projected area and mass. The distributions in Fig. 14b produce the same visible optical depths (by design). However, the sensitivity to theory is more pronounced. In the curve labeled "Columns", the results were obtained by using the collection efficiency corrected gamma distribution in Fig. 14b and the column crystal geometry shown in Fig. 12b (again, the visible optical depth is the column distribution gives a theoretical value of 0.214, same as the measured value and the plate calculations). The "Columns" model actually is better than the "Plates" model for wavenumbers below 950 cm^{-1} , but then it deviates much more from measurement beyond this wavenumber than the "Plates" model.

The "ADT" curve in Fig. 14c was obtained from the collection-efficiency- corrected gamma distribution in Fig. 14b, the plate crystal geometry in Fig. 12a, and with anomalous diffraction theory replacing the Mie theory for particle cross sections. ADT generally overestimates emission, especially for the small wavenumbers, but does better than Mie theory beyond about 1050 cm^{-1} . ADT generally gives absorption cross sections in excess of Mie theory

for small size parameters because ADT is a simple ray theory model most applicable at larger size parameters and refractive indices close to unity. Eventually for small size parameters, particle cross sections are largely similar to dipoles, and are modeled more accurately by the Mie theory. The sensitivity to theory displayed in Fig. 14c suggests that laboratory measurements are a useful guide in evaluating numerical methods for computing single particle scattering cross sections and for radiative transfer models.

4.4 EXPERIMENTAL RESULTS

Theoretical and experimental calculations for laboratory emission measurements agree well in some cases. Collection efficiency corrected observed cloudscope size distributions with no other adjustable parameters were used to calculate the theoretical spectra. The main situation that brought about disagreement between theory and observed FTIR measurements was when the particle concentration and optical depth were large.

High particle concentration usually occurred when numerous small ($< 5 \mu\text{m}$) crystals were observed. The errors in the cloudscope collection efficiency would be most significant at these small sizes. The crystal size spectra of the cloud is normalized and smoothed using the observed optical depth and the measured particle size distribution. If a large number of small particles went undetected, optical depth calculations could be in error, leading to errors in the theoretical calculations of emissivity.

Spectra (Fig. 15) from a day when the laboratory ice cloud was exceptionally consistent throughout the measurement period is described. The measurements shown are each an average of ten individual spectra (approximately 3 minutes time average), and were obtained over a 40-minute period. During this period the temperature of the cloud chamber rose slowly, and the cloud visible optical depth stayed very steady. Plate shaped crystals were observed on the cloudscope through the entire time period. The first measurement in the series is the spectra

discussed in Fig. 14a. The FTIR spectra taken during this time period appeared to be very similar. The number concentration increased and the mean diameter decreased as the cloud temperature increased. The visible optical depth increased slightly. The agreement of theory with measurement is reasonable during much of this series. The last measurement at -9.5 C was taken when the cloud had its highest concentration particles and the highest concentration of very small particles. This was also the measurement where there was the largest difference between theory and experimental results.

The next set of spectra for column crystal clouds demonstrates significant spectral shape differences for similar cloud temperatures. Spectra shown in Figs. 16a and 16b were obtained during a two minutes period while the cloud evolved rapidly. These clouds were of higher optical depth than the clouds in Fig. 15. The main difference between Figs. 16a and 16b lies in the different crystal size distributions. The first spectrum (Fig 16a) was taken when there were many more small crystals. When the second spectrum (Fig. 16b) was taken, the observed particles were much larger. Columns with an aspect ratio near unity ('squatty columns') were observed throughout the entire time period. The observed spectra are quite different.

For the smaller particles (Fig. 16a) the broad hump centered around 750 cm^{-1} was shifted towards the higher wavenumbers compared to the larger particle emission spectrum (Fig. 16b). The theoretical spectra did not agree well when single scattering was assumed. When multiple scattering was added into the theory, the theoretical spectra agreed much better. However, the theoretical spectra disagree with their respective experimental spectra by a much greater amount than in the previous examples of Fig. 15. The shapes of the curves are worth note. The theoretical curves do not mimic the experimental curves very well in shape. The difference in location of the 750 cm^{-1} hump is predicted with the theoretical calculations though. It is possible that these measurements at higher optical depth are contaminated by room temperature emission

entering the FTIR view port in Fig. 5 that backscatters to the spectrometer. This emission has not been added to the theoretical model.

Cloud temperature plays a large role in the emission spectrum. The next two spectra (Figs. 17a, 17b) were obtained at two different temperatures, and thus two different crystal growth regions and emission strengths. The visible optical depths were 0.60 and 0.45. The temperatures were -15 and -6 , which led to growth of plates and columns, respectively. The theoretical spectra agreed well in shape, but again poorly in magnitude.

5. APPLICATIONS IN THE ATMOSPHERE

In this section atmospheric applications are explored by expanding on the model results presented in Fig 16a. The error in using single scattering or zero scattering approximations are presented along with model derived "LIRAD" ratios.

Some connections between theory and intuition can be accomplished by considering several limits. The fractional error in cloud emission (not considering emission from the walls) found by considering only one scattering event is obtained from Eq. (3) and Eq. (6) as

$$\Delta_{ss} = -\frac{\beta_{sca}}{\beta_{ext}}(1 - \exp(-\beta_{ext}L)) \quad , \quad (24)$$

where Δ_{ss} is the single scattering solution minus the multiple scattering solution (presumed correct) all divided by the multiple scattering solution. Note that while the single scattering solution generally under estimates cloud emission, it only does so when the single scattering albedo $\omega = \beta_{sca}/\beta_{ext}$ and the optical depth $\beta_{ext}L$ are appreciably different from zero. In other words, the single scattering approximation is reasonable when the single scattering albedo and/or the optical depth are $\ll 1$. Figure 18a shows this error as a function of wavenumber. Note that

the error approaches 50%, and is smallest where the real part of the refractive index of ice is close to unity.⁹

The so-called zero scattering approximation is often made in evaluating cloud emission for climate models and remote sensing applications.¹⁸⁻²⁰ This approximation can be reached simply by setting $\beta_{ext} = \beta_{abs}$ and $\beta_{sca} = 0$ in Eq. (6), giving

$$I_c^{zs}(\nu) = B(T_c, \nu) [1 - \exp(-\beta_{abs}(\nu)L)]. \quad (25)$$

The fractional error, Δ_{zs} , in using the zero scattering approximation (not considering emission from the walls) is obtained from Eq. (6) and Eq. (25) as

$$\Delta_{zs} = \frac{I_c^{zs}(\nu) - I_c(\nu)}{I_c(\nu)}. \quad (26)$$

As shown in Fig. 18a, the zero scattering approximation results in an error of between about 4% and 26%, and the approximation underestimates emission. The error in the gaseous atmospheric window region between 650 cm^{-1} and 1250 cm^{-1} (i.e. $8 \text{ }\mu\text{m}$ and $15 \text{ }\mu\text{m}$) are below 18%, and reach a minimum near a wavenumber of 950 cm^{-1} . Figure 18b shows the model extinction (gas and particle) and scattering (particle) optical depths. It is not surprising that the minimum error in the zero scattering approximation occurs at the minimum in the scattering optical depth. The scattering and reflection components of measured emittance by tropical atmospheres have also been shown to be appreciable.²¹

A useful measure of cloud microphysics can be obtained from remote sensing measurements using a visible wavelength lidar and a infrared radiometer (i.e. the LIRAD method).¹⁹ The lidar and radiometer are used to estimate the local visible optical depth and IR absorption optical depth in a narrow band centered at a wavelength (wavenumber) of $10.85 \text{ }\mu\text{m}$ (921.66 cm^{-1}). The LIRAD ratio is generally smaller (less than 2) when no small ice crystals are

present ($< 100 \mu\text{m}$ maximum dimension), and grows as their numbers increase. Figure 19a and 19b show the model spectrally resolved LIRAD ratio both as function of wavenumber and wavelength. The ratio approaches 5 in the atmospheric window region. Atmospheric measurements have shown ratios this large, and even larger. Keep in mind that the size spectrum of plate ice crystals used to obtain these theoretical results is the column spectra on the inset of Fig. 16a. The mean crystal height was $10.9 \mu\text{m}$. In a gross sense, the LIRAD ratio is the second (area) moment of the particle size distribution (psd) divided by a weighted sum of the second and third moments (volume) of the psd, with the emphasis on the volume when particles are $\ll 100 \mu\text{m}$, and area otherwise. LIRAD is a useful tool for remotely sensing properties of the psd when direct in situ observation is not possible. Recently reported values of this ratio for tropical cirrus were generally larger than the value of 2.42 at $10.85 \mu\text{m}$ found here.¹⁹ One implication is that tropical cirrus has huge numbers of very small ice crystals.

Summarizing the results of this section, don't use the single scattering approximation. The zero scattering approximation is not horrible, but perhaps could be improved upon by using Eq. (6) with $L_w = L =$ (cloud layer thickness) in an atmospheric context. The relative minimum in the extinction curve has been observed in a cloud hypothesized to contain large numbers of small ice crystals.⁷ The theory presented here, as evaluated with measurements, provides a useful framework for interpreting atmospheric measurements.

6. CONCLUSION

Measurements of laboratory ice cloud emission have been performed and modeled with modified Mie theory. The crystal size distribution was measured simultaneously, and used directly in the model. Model and measured spectra generally were in reasonable agreement, indicating that modified Mie theory is useful for computing the cross sections for absorption and

extinction for ice crystals in the infrared. That is not to say that modified Mie theory is useful for other properties of ice clouds such as the degree of polarization and the angular scattering phase functions. However, since these cross sections are a rather gross particle property, it is most important to properly model the particle physical cross section and volume (mass), and to have accurate knowledge of the particle refractive index. The expression used to obtain absorption and extinction coefficients in Eq. (21) is essentially a matrix formulation where a 2-D kernel matrix with all wavenumbers and particle sizes is computed once at the outset, and is multiplied by the 1-D particle size distribution to obtain coefficients. This matrix formulation should also be useful when generating computational results from computationally expensive non spherical particle scattering theory. These measurements are also useful in evaluating different models for infrared radiative transfer, as has been demonstrated in Sec. 5.

ACKNOWLEDGEMENTS

This work was supported by the National Science Foundation, grant ATM-9413437. We are grateful to Jane Niehuss-Brooks for assistance with cloudscope data analysis. Development of the cloudscope data analysis tools was supported by the National Aeronautics and Space Administration, grant NAG-2-1104.

REFERENCES

1. Baumgardner, D. and Gandrud, B. E., A comparison of the microphysical and optical properties of particles in an aircraft contrail and mountain wave cloud. *Geophysical Research Letters*, 1998, **25**, 1129-1132.
2. Goodman, J., Pueschel, R. F., Jensen, E. J., Verma, S., Ferry, G. V., Howard, S. D., Kinne, S. A. and Baumgardner, D., Shape and size of contrail ice particles. *Geophysical Research Letters*, 1998, **25**, 1327-1330.
3. Heymsfield, A. J., Ice particles observed in a cirriform cloud at -83 C and implications for polar stratospheric clouds. *Journal of the Atmospheric Sciences*, 1986, **43**, 851-855.
4. Prabhakara, C., Kratz, D. P., Yoo, J. M., Dalu, G. and Vernekar, A., Optically thin cirrus clouds: Radiative impact on the warm pool. *Journal of Quantitative Spectroscopy and Radiative Transfer*, 1993, **49**, 467-483.
5. Fu, Q. and Liou, K. N., Parameterization of the radiative properties of cirrus clouds. *Journal of the Atmospheric Sciences*, 1993, **50**, 2008-2025.
6. Jensen, E. J., Kinne, S. and Toon, O. B., Tropical cirrus cloud radiative forcing: Sensitivity studies. *Geophysical Research Letters*, 1994, **21**, 2023.
7. Smith, W. L., Ackerman, S., Revercomb, H., Huang, H., DeSlover, D. H., Feltz, W., Gumley, L. and Collard, A., Infrared spectral absorption of nearly invisible cirrus clouds. *Geophysical Research Letters*, 1998, **25**, p. 1137.
8. Prabhakara, C., Yoo, J.-M., Dalu, G. and Fraser, R. S., Deep optically thin cirrus clouds in polar regions. Part 1. Infrared extinction characteristics. *Journal of Applied Meteorology*, 1990, **29**, 1313-1329.

9. Arnott, W. P., Dong, Y. Y. and Hallett, J., Extinction efficiency in the infrared (2-18 μ m) of laboratory ice clouds: observations of scattering minima in the Christiansen bands of ice. *Applied Optics*, 1995, **34**, 541-551.
10. Yang, P., Liou, K. N. and Arnott, W. P., Extinction efficiency and single-scattering albedo for laboratory and natural cirrus clouds. *Journal of Geophysical Research*, 1997, **102**, 21825-21835.
11. Best, P. E., Carangelo, R. M., Markham, J. R. and Solomon, P. S., Extension of emission-transmission technique to particulate samples using FT-IR. *Combustion and Flame*, 1986, **66**, 47-66.
12. Bryant, F. D. and Latimer, P., Optical efficiencies of large particles of arbitrary shape and orientation. *Journal of Colloid and Interface Science*, 1969, **30**, 291-304.
13. Mitchell, D. L. and Arnott, W. P., A Model Predicting the Evolution of Ice Particle Size Spectra and Radiative Properties of Cirrus Clouds. Part II: Dependence of Absorption and Extinction on Ice Crystal Morphology. *Journal of the Atmospheric Sciences*, 1994, **51**, 817-832.
14. Fu, Q., Yang, P. and Sun, W. B., An Accurate Parameterization of the Infrared Radiative Properties of Cirrus Clouds for Climate Models. *Journal of Climate*, 1998, **11**, 2223-2237.
15. Warren, S. G., Optical constants of ice from the ultraviolet to the microwave. *Applied Optics*, 1984, **23**, 1206-1225.
16. Wolfe, W. L. and Zissis, G. J., *The Infrared Handbook*, Vol. The Infrared Information Analysis Center, Washington DC, 1993, pp.
17. Langmuir, I., *The Collected Works of Irving Langmuir*, Vol. 10. Pergamon Press, New York, 1961, pp. 354-372.

18. Stephens, G. L., Tsay, S.-C., Jr., P. W. S. and Flatau, P. J., The relevance of the microphysical and radiative properties of cirrus clouds to climate and climatic feedback. *Journal of the Atmospheric Sciences*, 1990, **47**, 1742-1753.
19. Platt, C. M. R., Young, S. A., Manson, P. J., Patterson, G. R., Marsden, S. C., Austin, R. T. and Churnside, J. H., The Optical Properties of Equatorial Cirrus from Observations in the ARM Pilot Radiation Observation Experiment. *Journal of the Atmospheric Sciences*, 1998, **55**, 1977-1996.
20. Chylek, P., Damiano, P. and Shettle, E. P., Infrared Emittance of Water Clouds. *Journal of the Atmospheric Sciences*, 1992, **49**, 1459-1472.
21. Platt, C. M. R. and Stephens, G. L., The interpretation of remotely sensed high cloud emittances. *Journal of the Atmospheric Sciences*, 1980, **37**, 2314-2322.

FIGURE CAPTIONS

Fig. 1. Schematic representation of the laboratory arrangement.

Fig. 2. Schematic of the warm reference blackbody.

Fig. 3. Schematic of the infrared spectrometer and calibration blackbodies. The room temperature blackbody is horizontal, and the warm temperature blackbody is vertical for thermal stability.

Fig. 4. Schematic of the target blackbody.

Fig. 5. Side view schematic of the laboratory arrangement.

Fig. 6. Measured air temperature profiles in the chamber.

Fig. 7. Schematic of the liquid nitrogen cloud seeder.

Fig. 8. Schematic of the cloudscope used to observe ice crystals.

Fig. 9. Theoretical correction efficiency curve for the cloudscope.

Fig. 10. Example of some observed plate and column ice crystals.

Fig. 11. Example of some ice crystals that landed on edge and tipped over.

Fig. 12. Measured crystal geometry for (a) plates and (b) columns.

Fig. 13. Radiance measurement when no ice cloud was present showing gaseous emission.

Fig. 14. (a) The top panel shows emissivity and the wavelength scale. The lower panel shows measured radiance (black curve), theoretical radiance (gray curve), and the theoretical contribution of wall radiance scattered by crystals into the spectrometer (as labeled wall). (b) The raw and collection efficiency corrected measured size distributions along with the gamma distribution curve fits. (c) Errors for the various theories when compared with the measurements. The curves labeled plates and plates, raw and columns are modified Mie theory for the size distributions in (b) and the crystal geometry in Fig. 12a and 12b, respectively. The curve labeled ADT was modified anomalous diffraction theory and was for the same configuration as the plates curve.

Fig. 15. A series of measurements (black curves) and theory (gray curves) for plate crystals (modified Mie theory) for the indicated temperatures, optical depths, and measured particle size spectra. Parameters of the gamma distribution fit are shown on the inlay size spectra graphs.

Fig. 16. Measured (black curves) and modeled (gray curves) emission spectra for column clouds having the indicated size spectra, cloud temperatures, and visible optical depths (OD).

Fig. 17. High optical depth plate (a) and column (b) cloud emission spectra for the indicated size spectra.

Fig. 18. Theoretical results for the correction efficiency corrected size spectra shown in Fig. 16a. (a) Errors in using the single zero scattering approximations, and (b), model derived extinction and absorption spectral optical depths.

Fig. 19. Model derived results for the ratio of visible optical depth to spectral absorption optical depth ("LIRAD" ratio) for the corrected size spectra shown in Fig. 16a. (a) shows the ratio as a function of wavenumber, and (b) shows it as a function of wavelength. The point singled out is at the the nominal wavelength of frequently used radiometers.

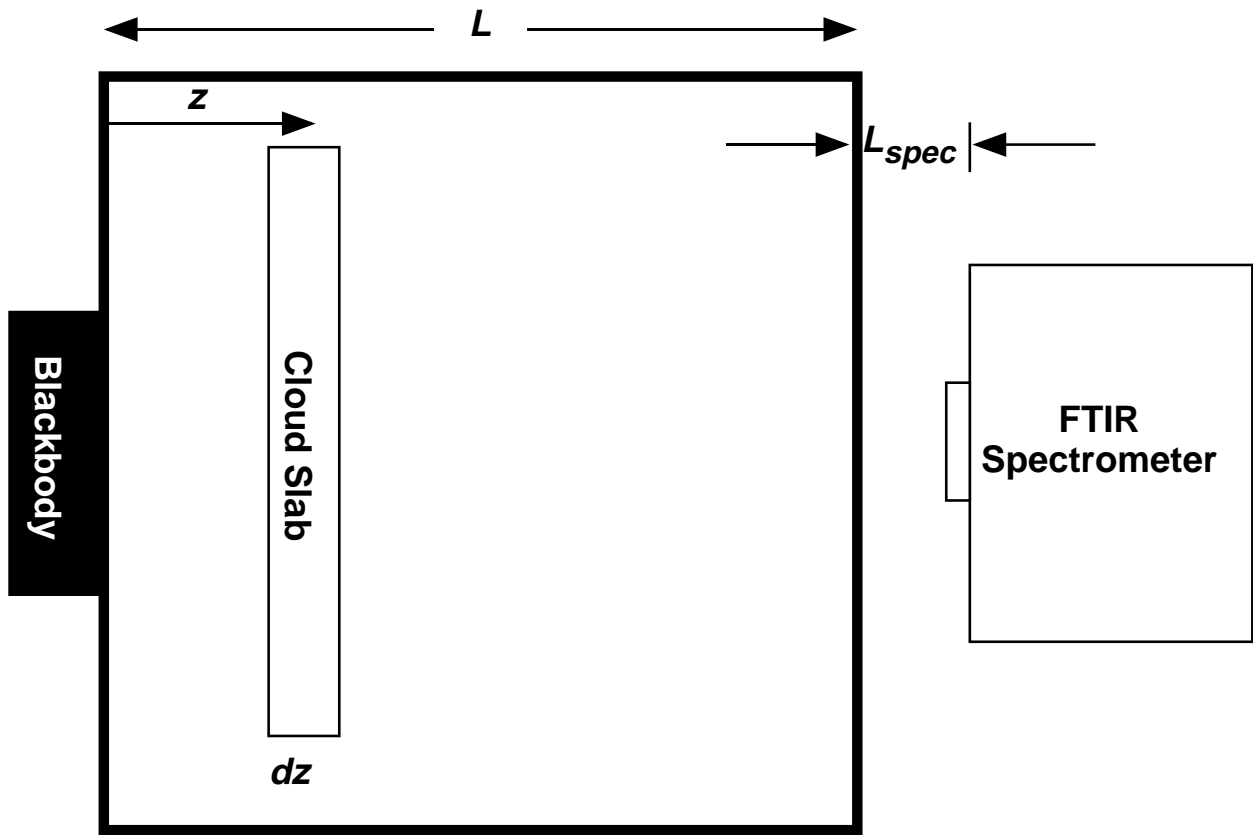


Figure 1.

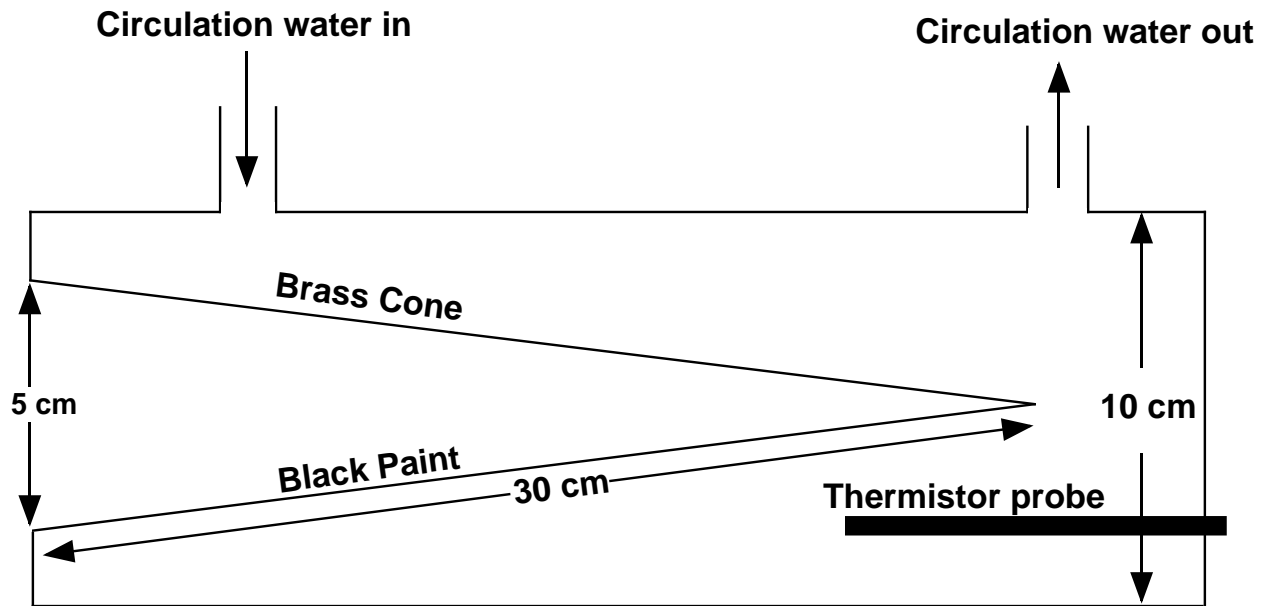


Figure 2.

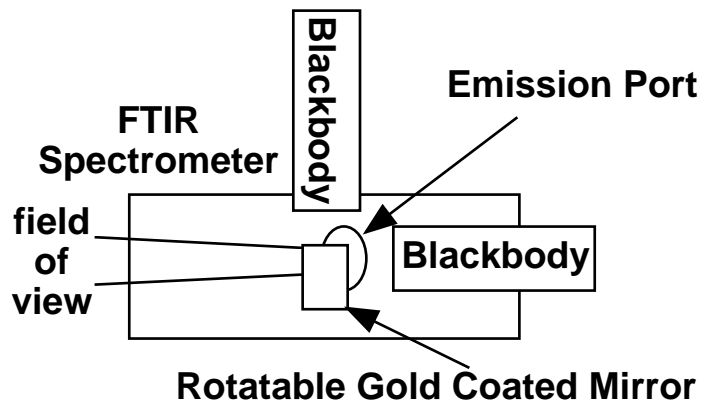


Figure 3.

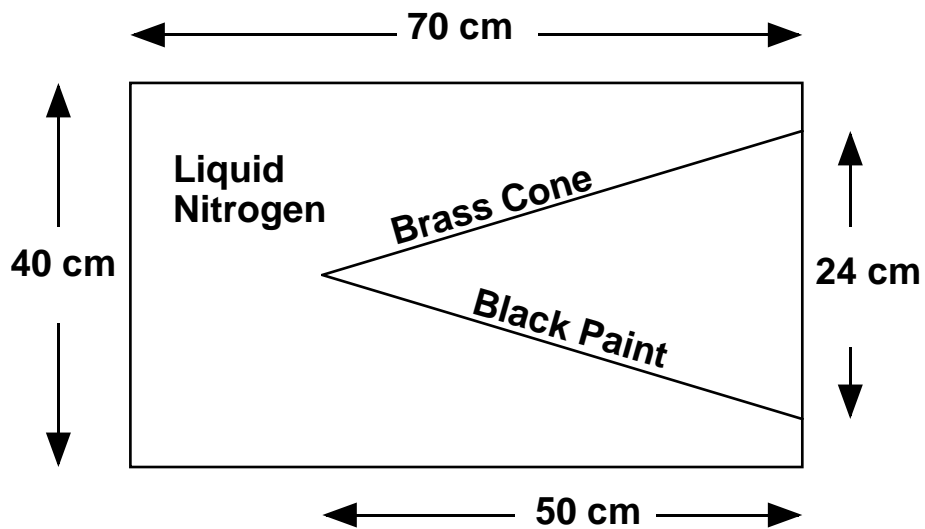


Figure 4.

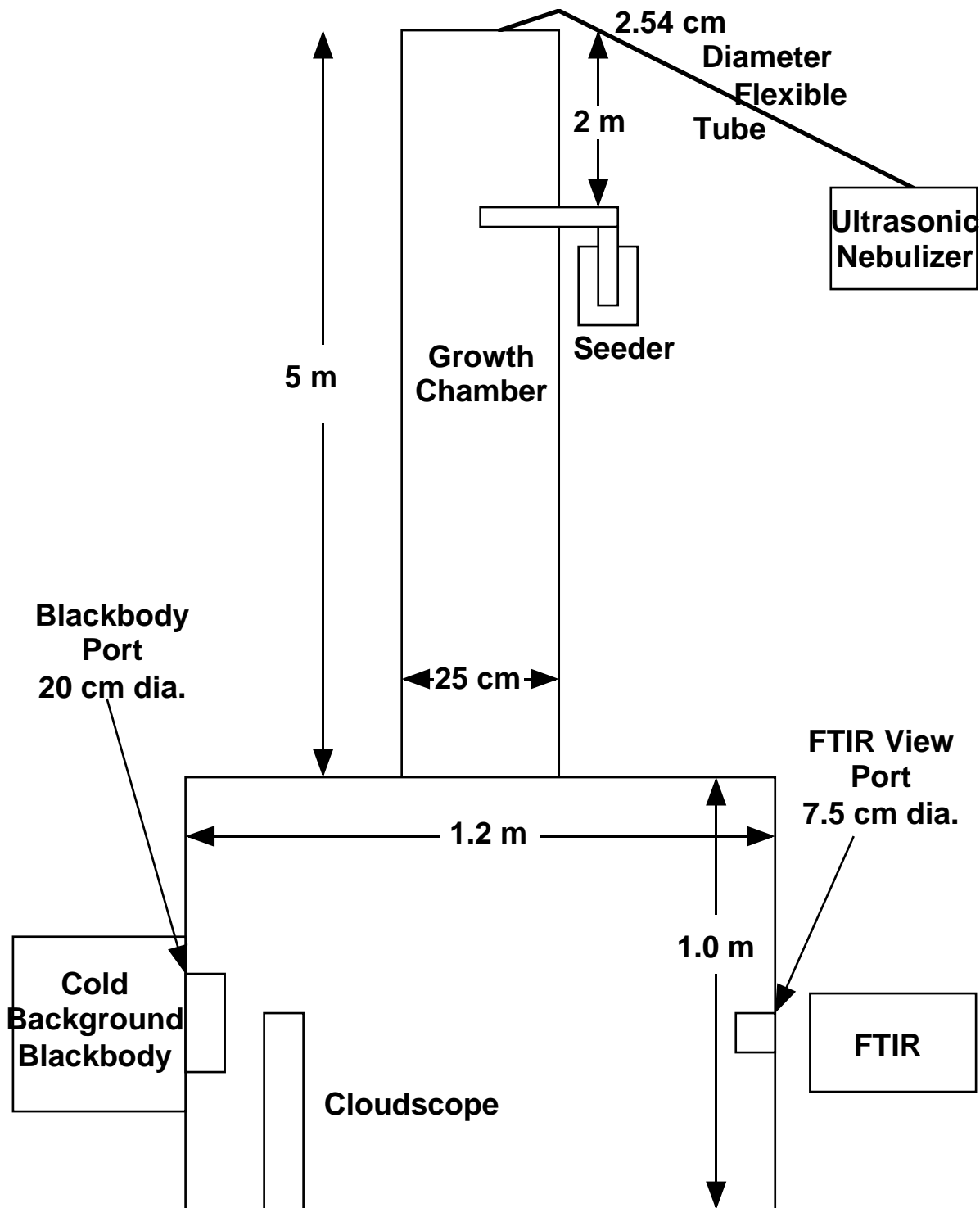


Figure 5.

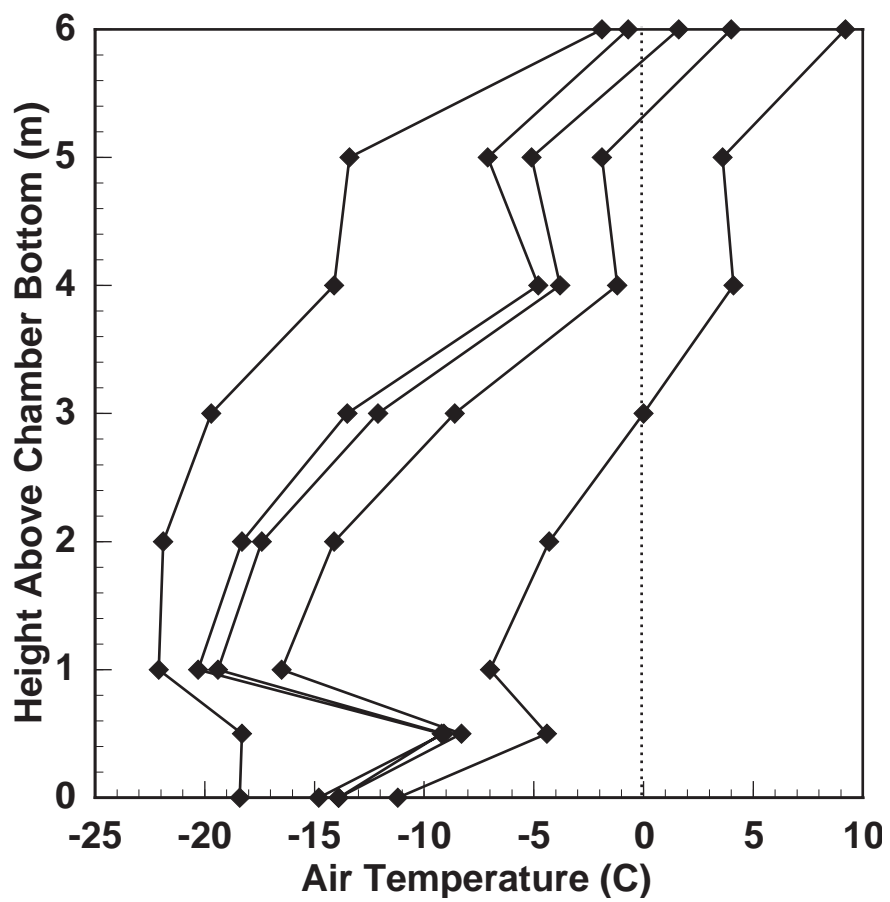


Figure 6.

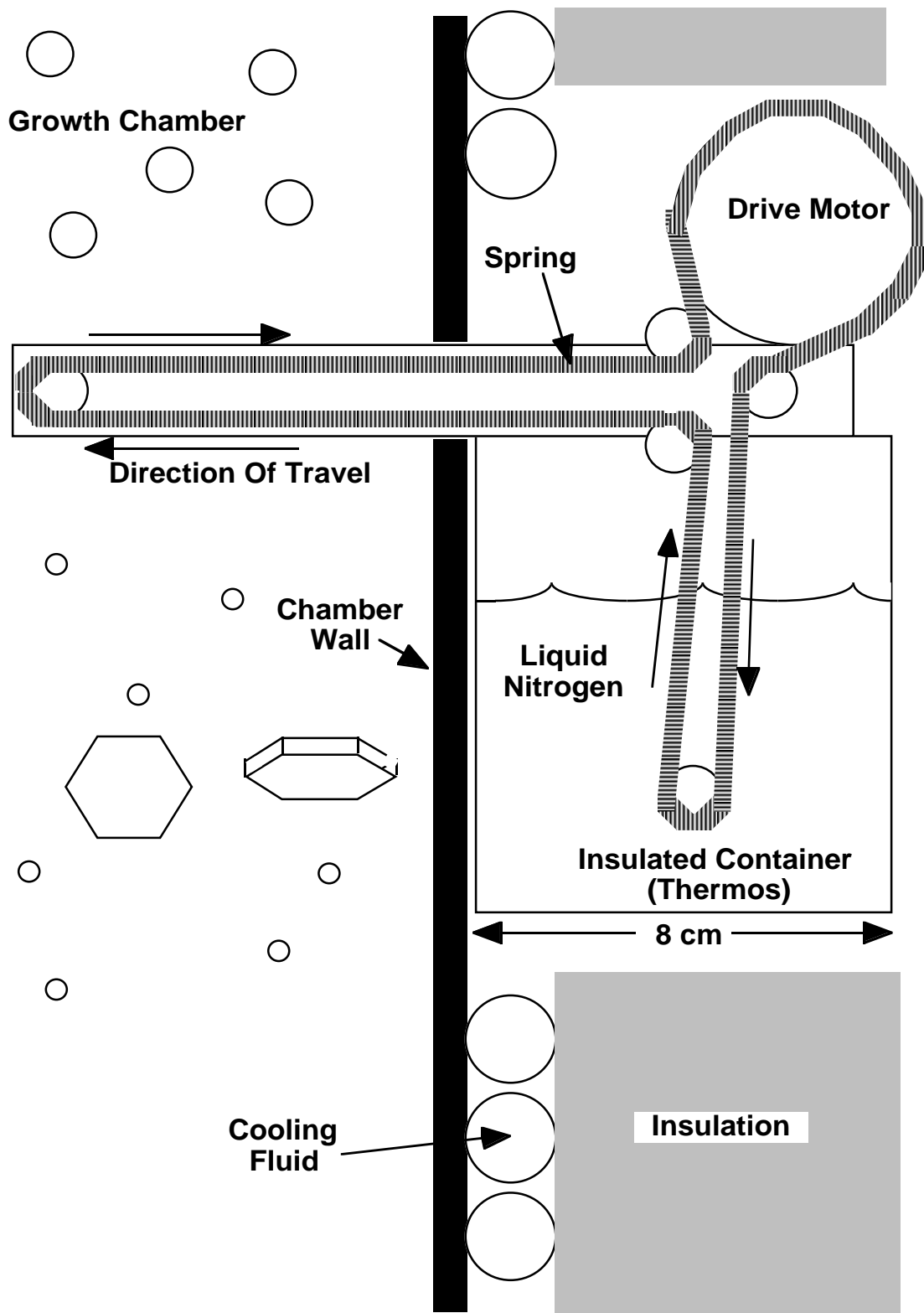


Figure 7.

Cloudscope

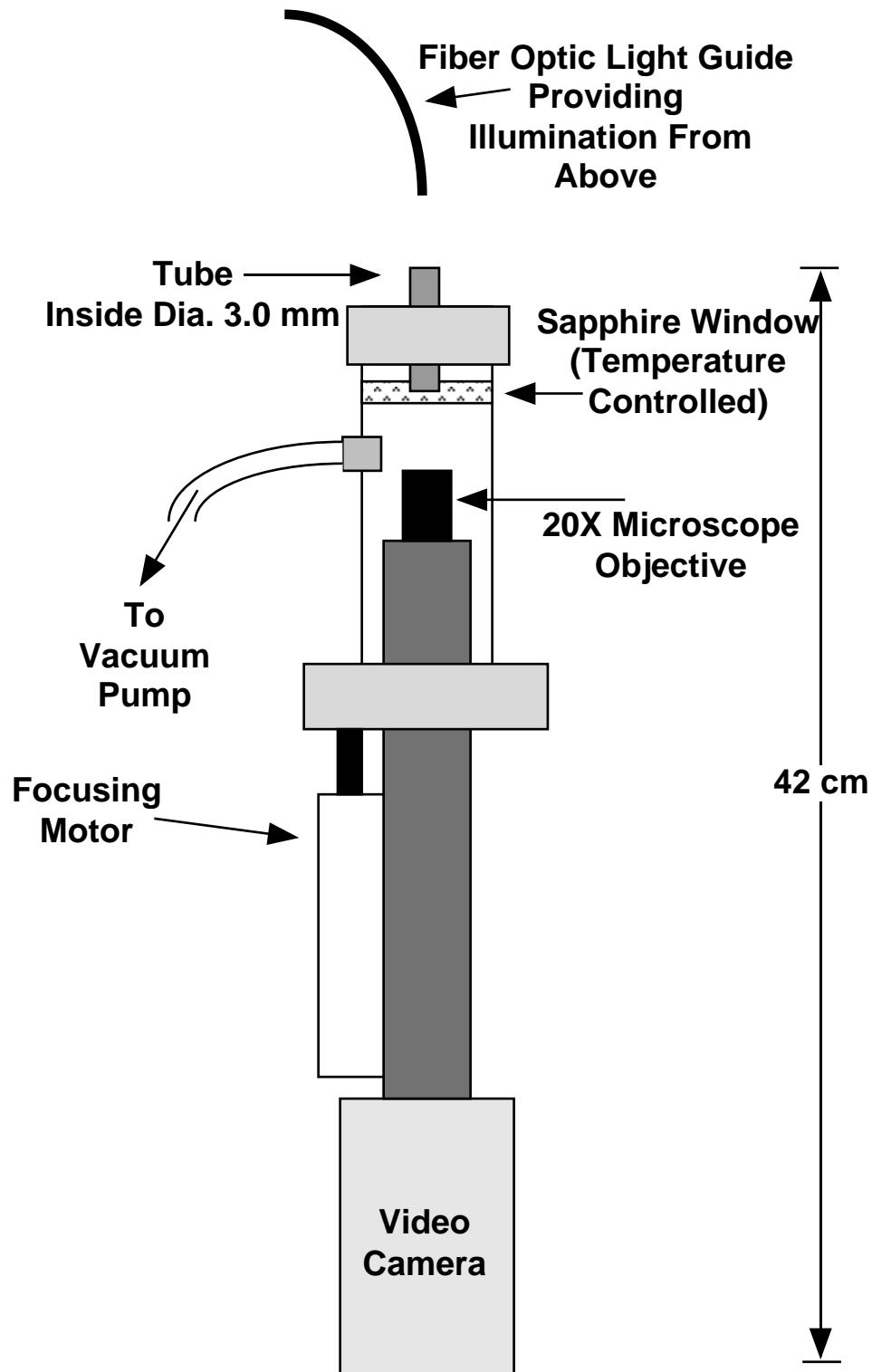


Figure 8.

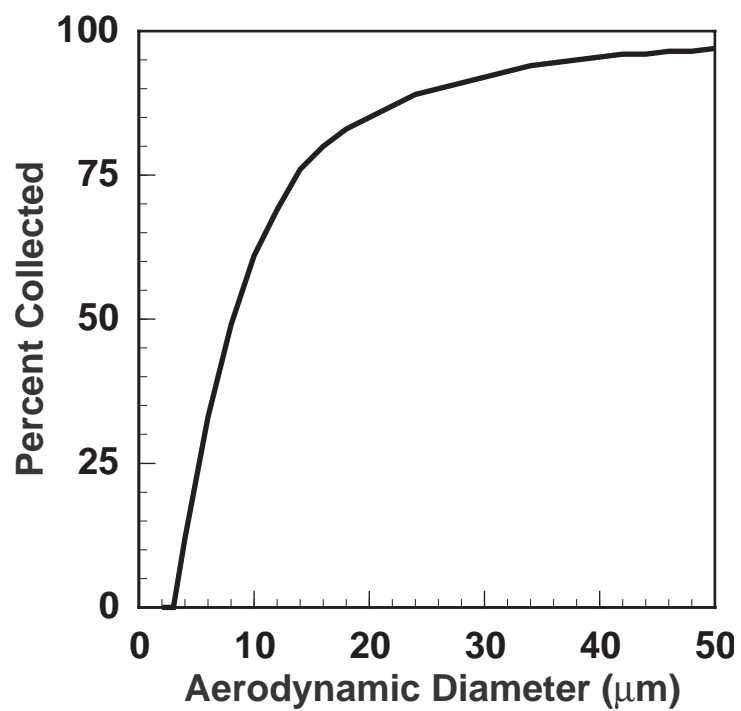


Figure 9.

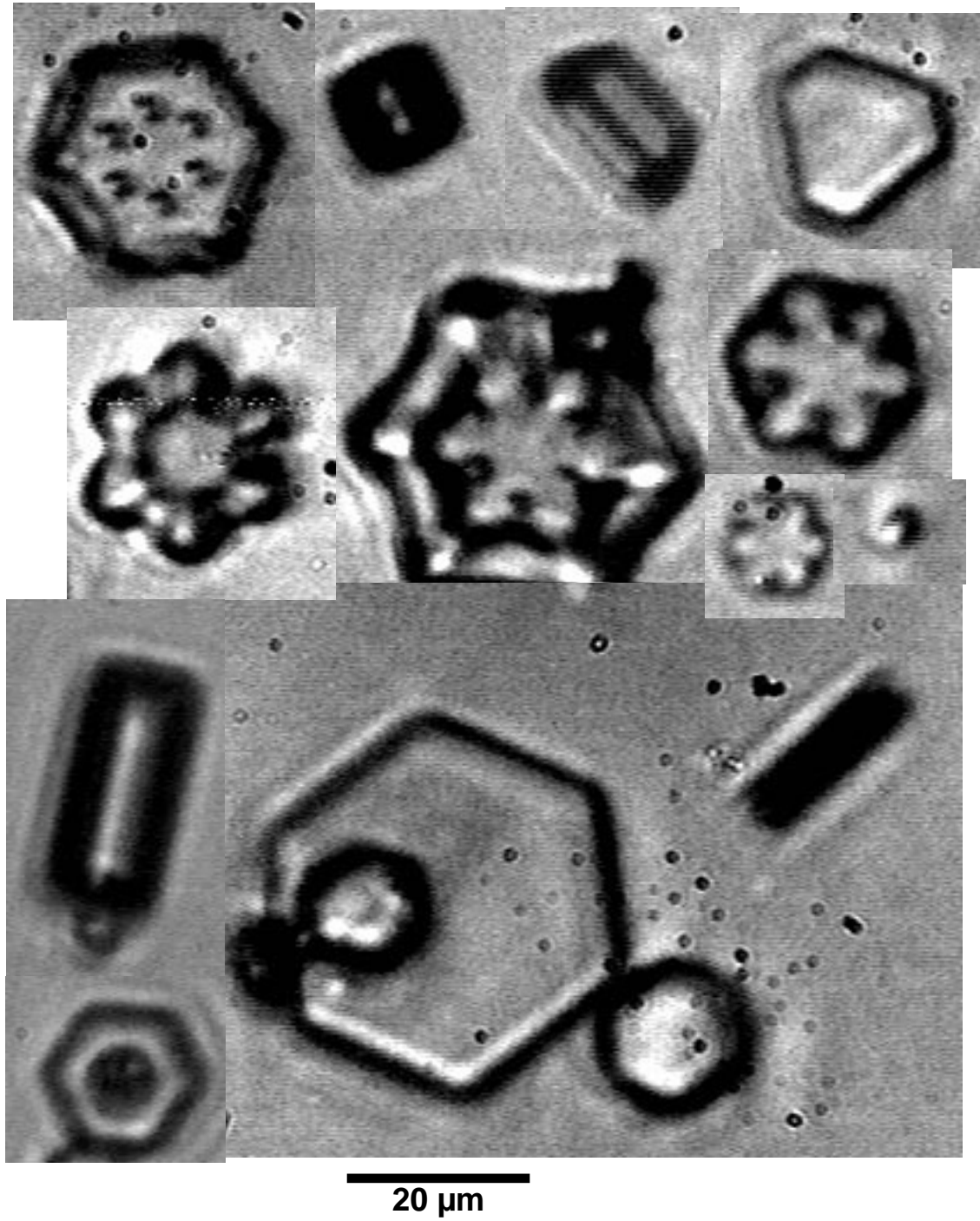


Figure 10.

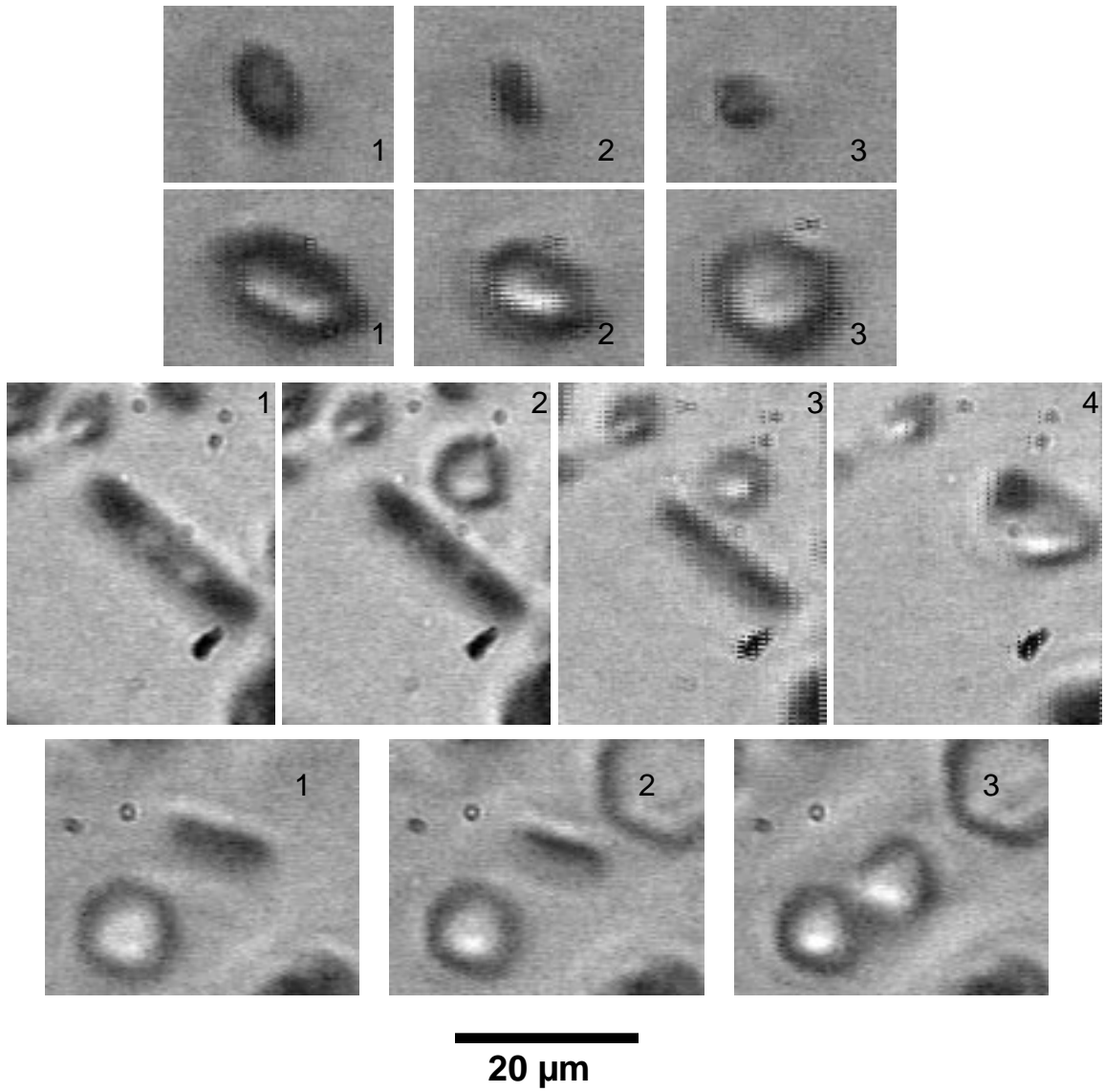


Figure 11.

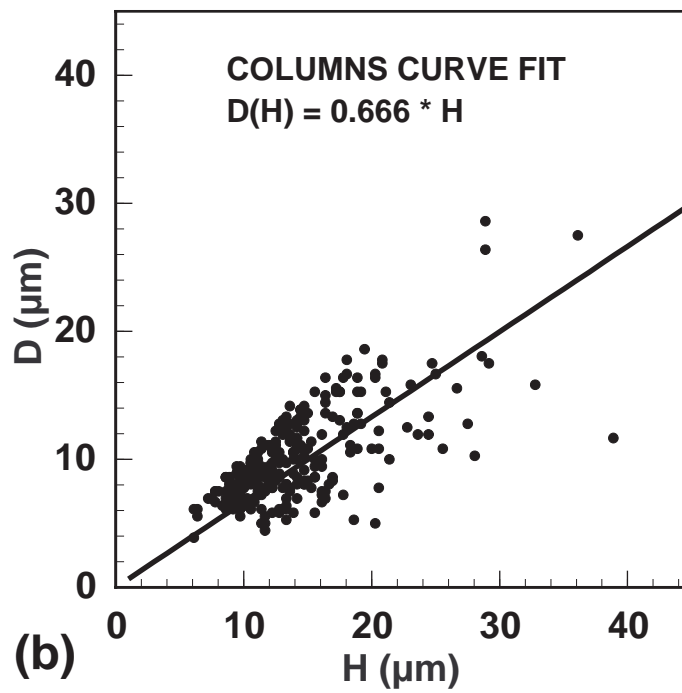
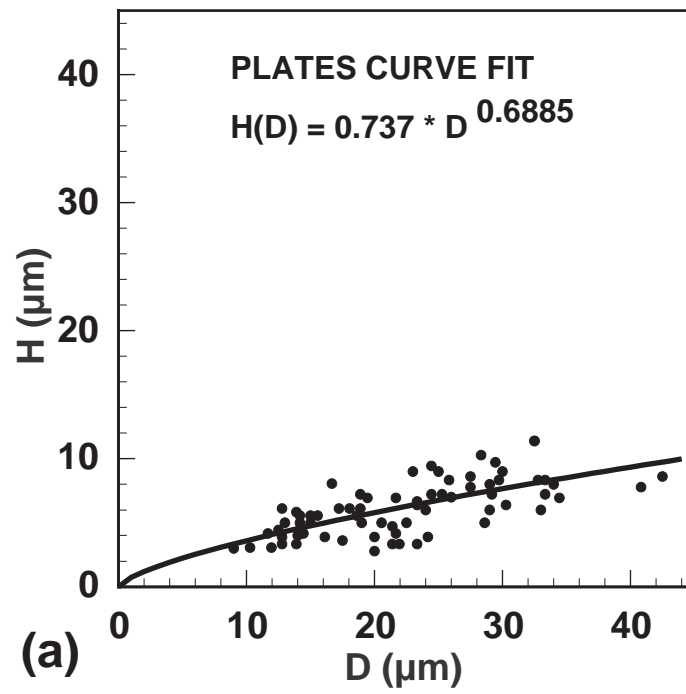


Figure 12.

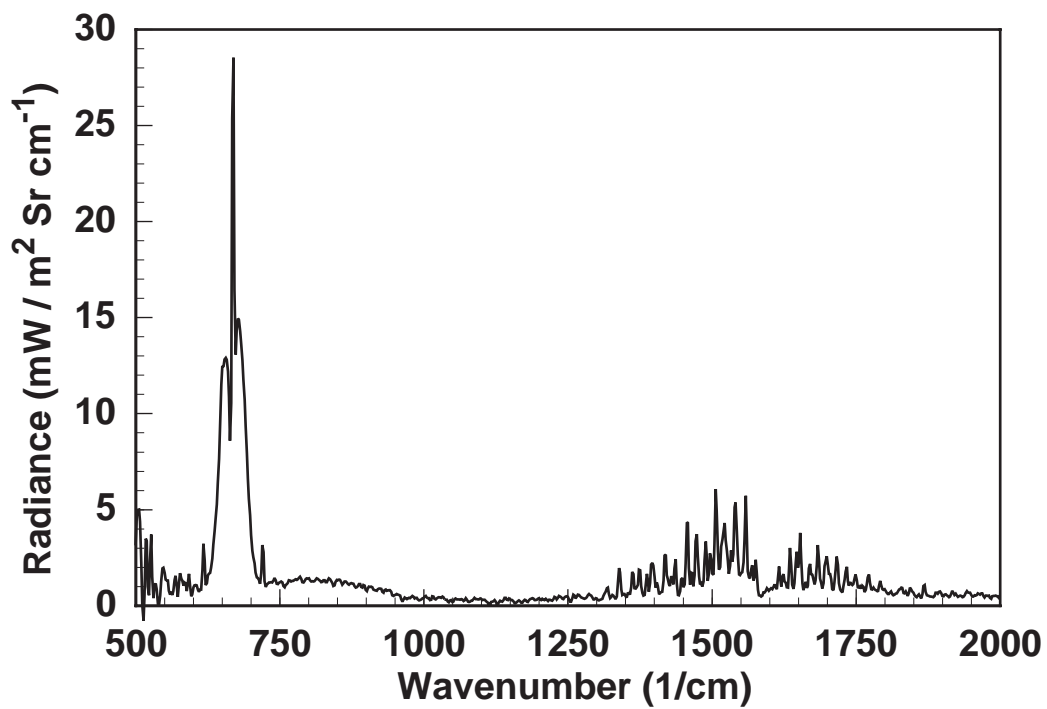


Figure 13.

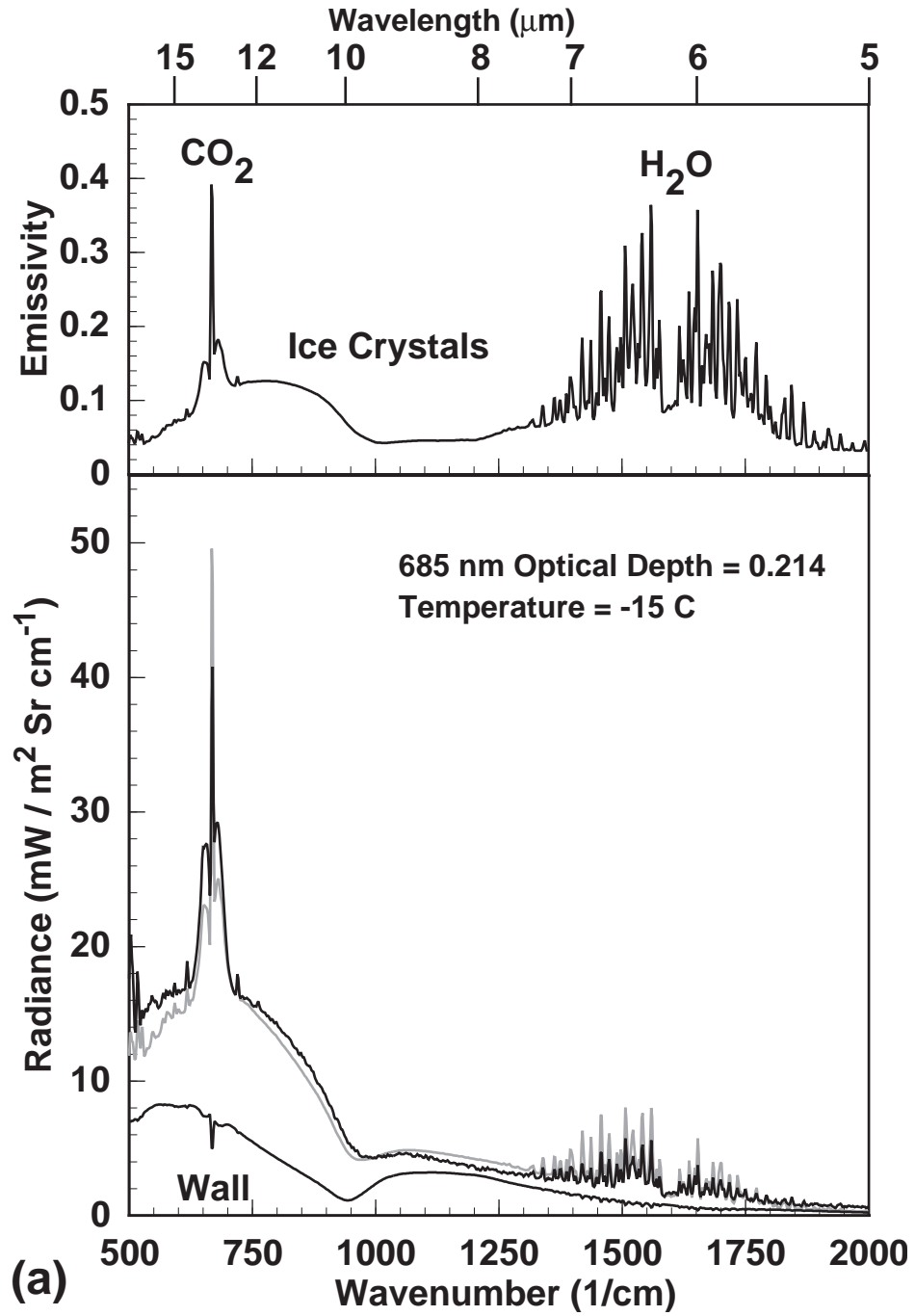


Figure 14a.

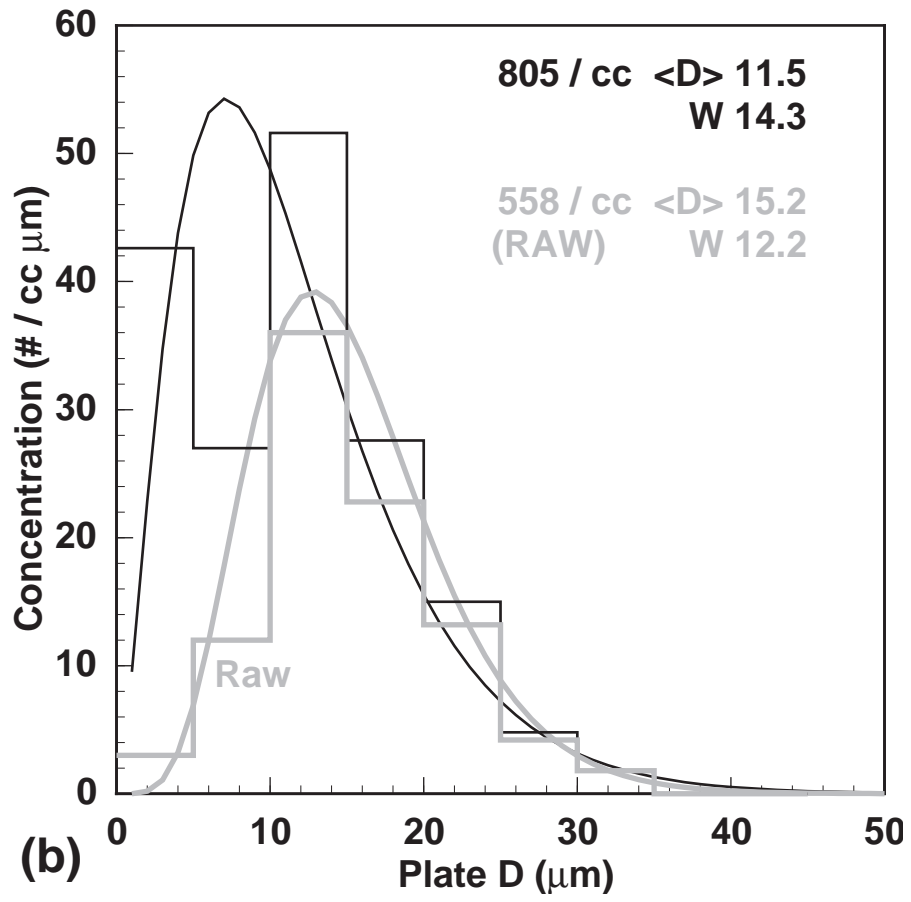


Figure 14b.

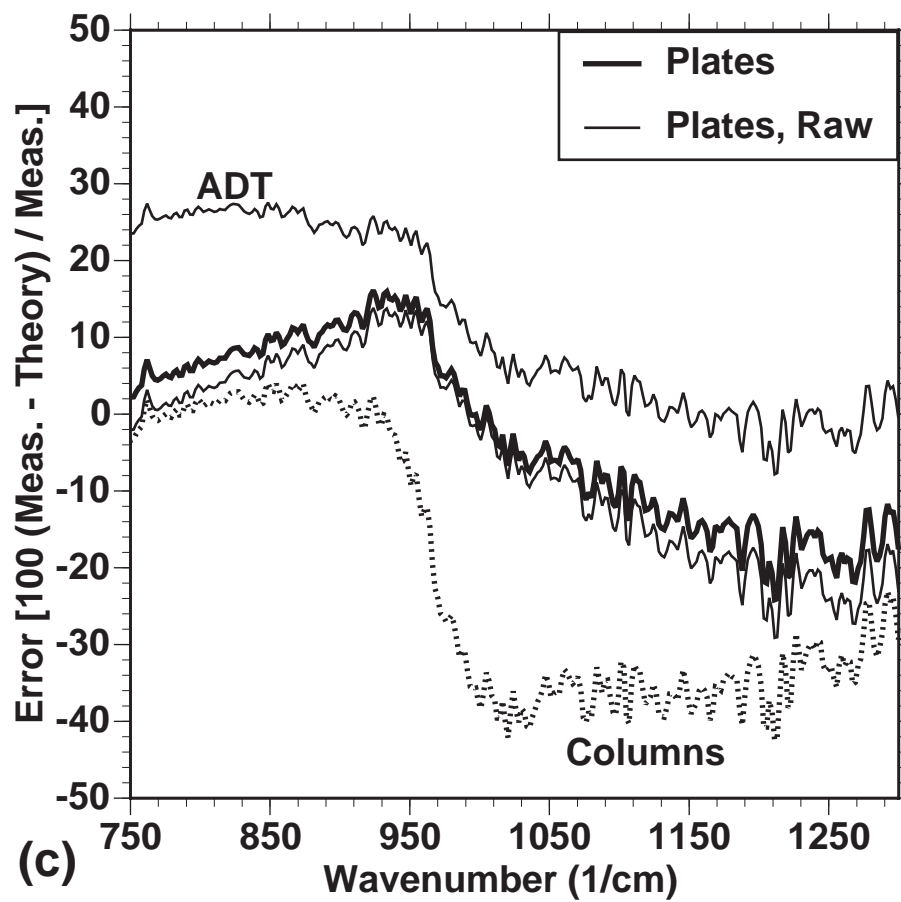


Figure 14c.

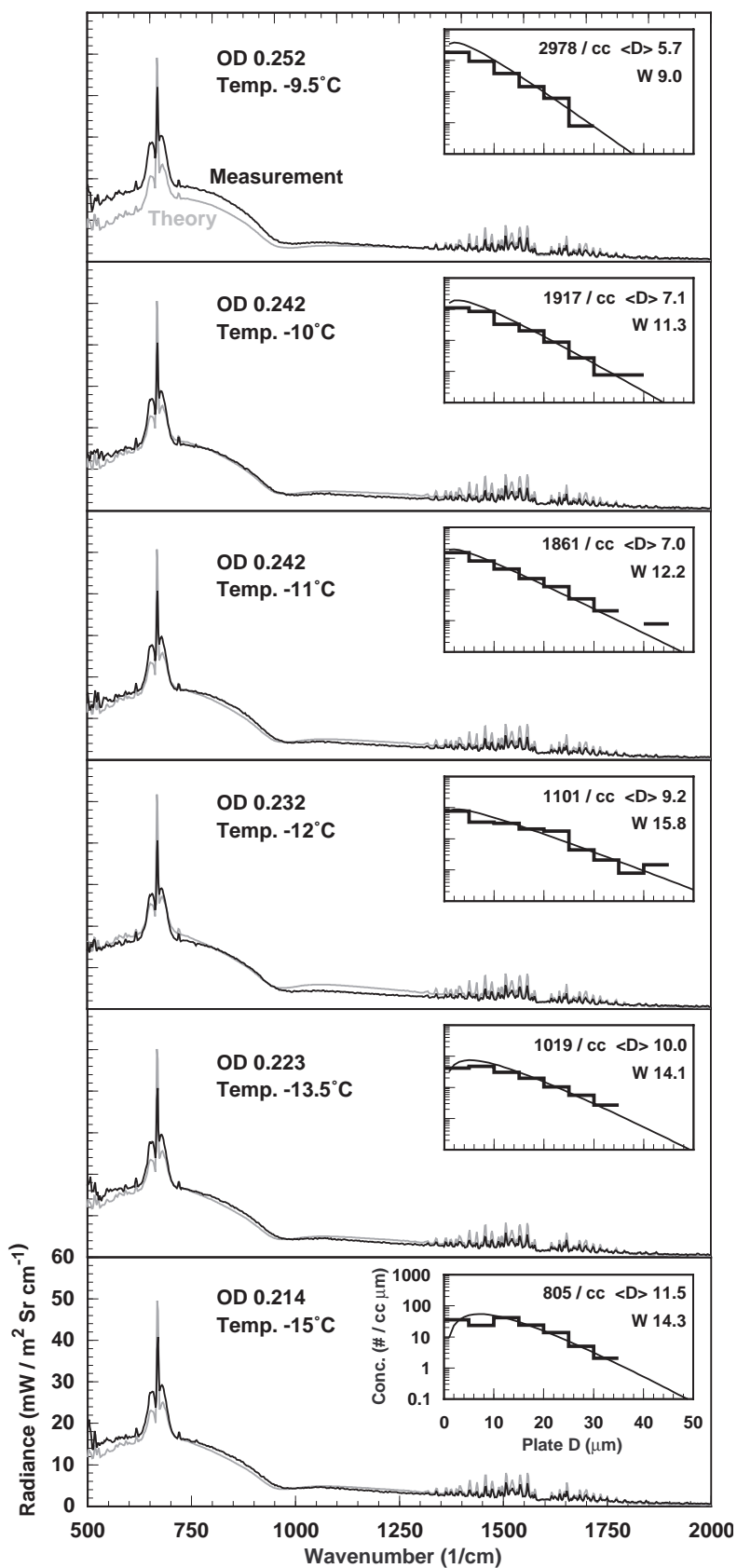


Figure 15

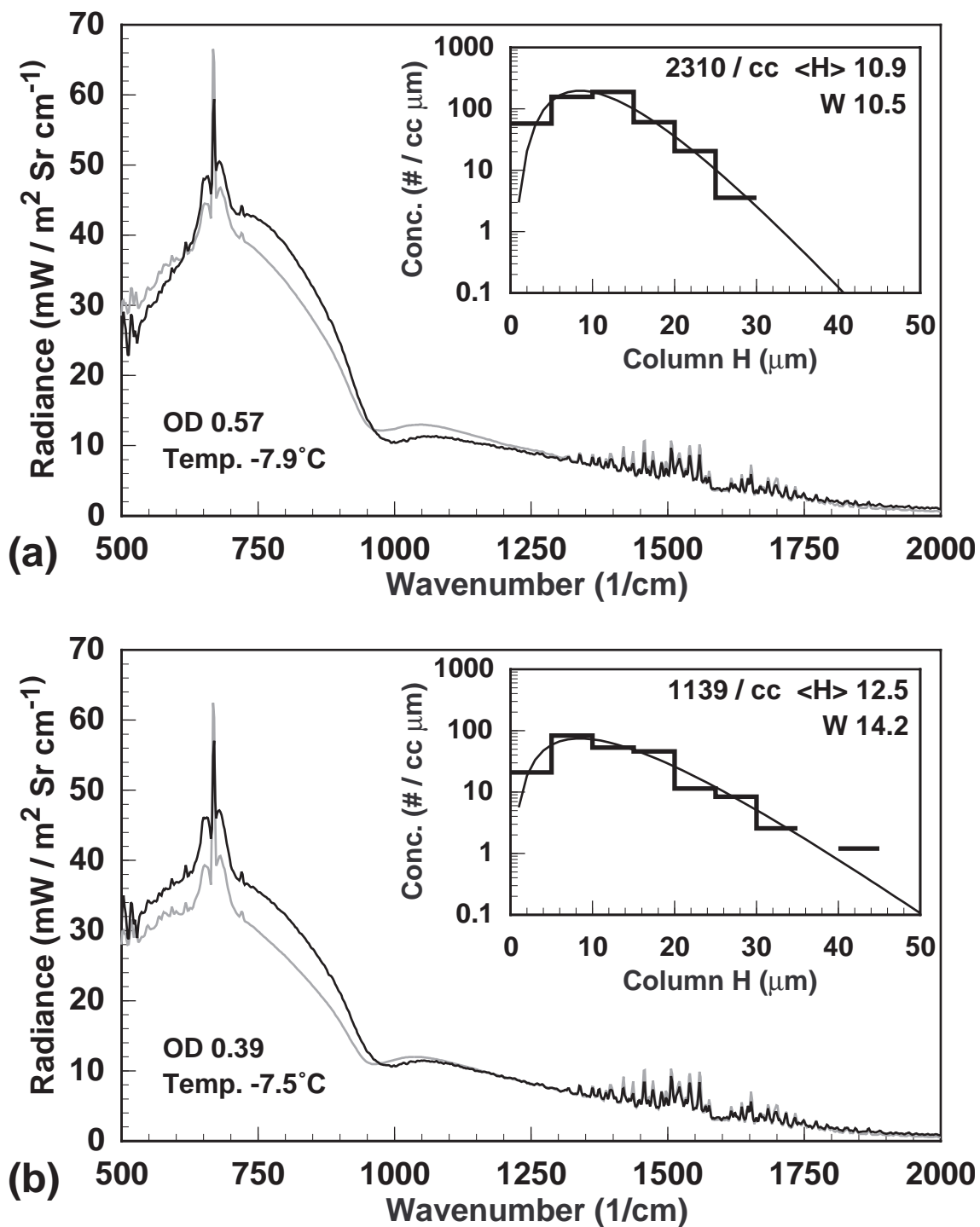


Figure 16.

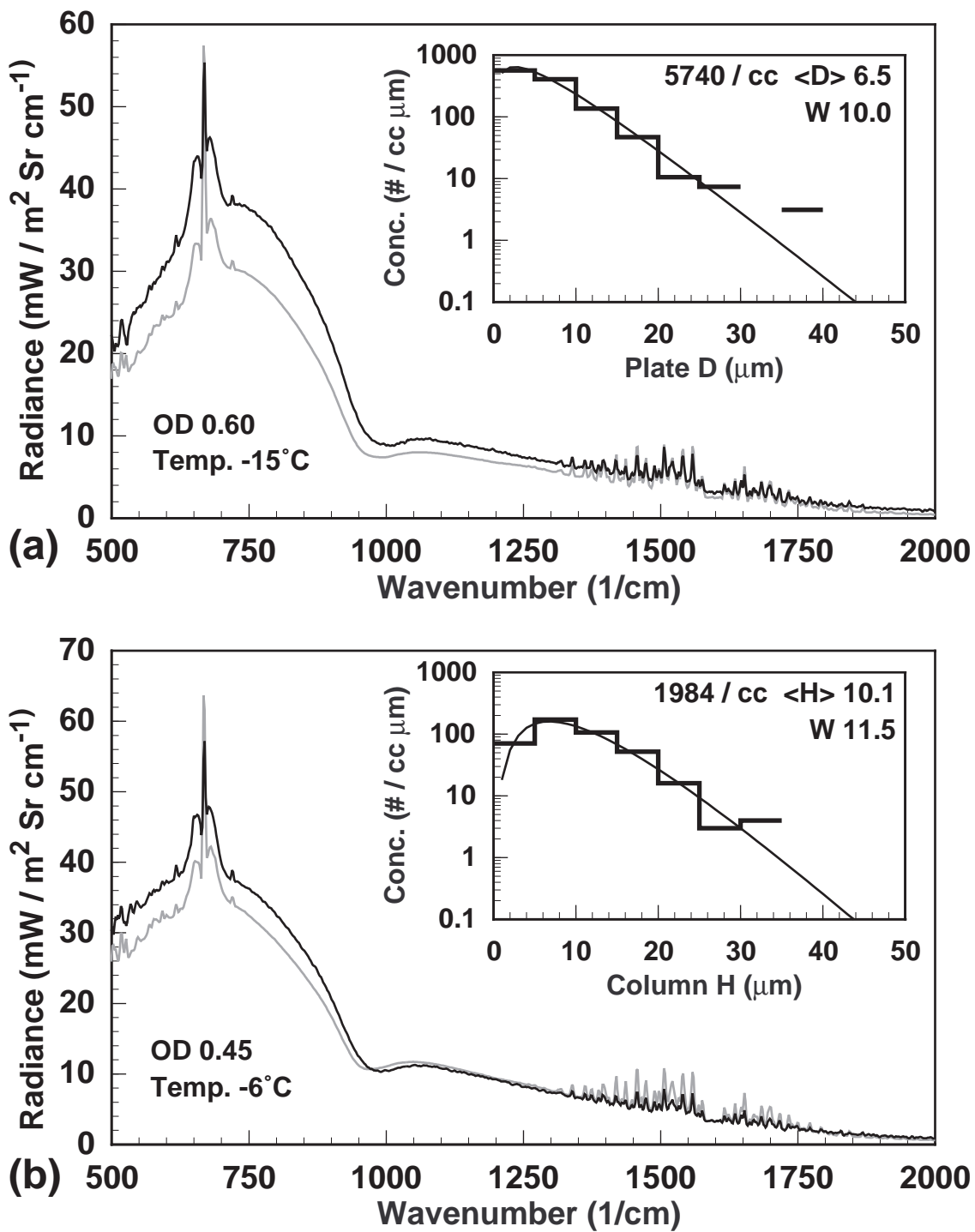


Figure 17.

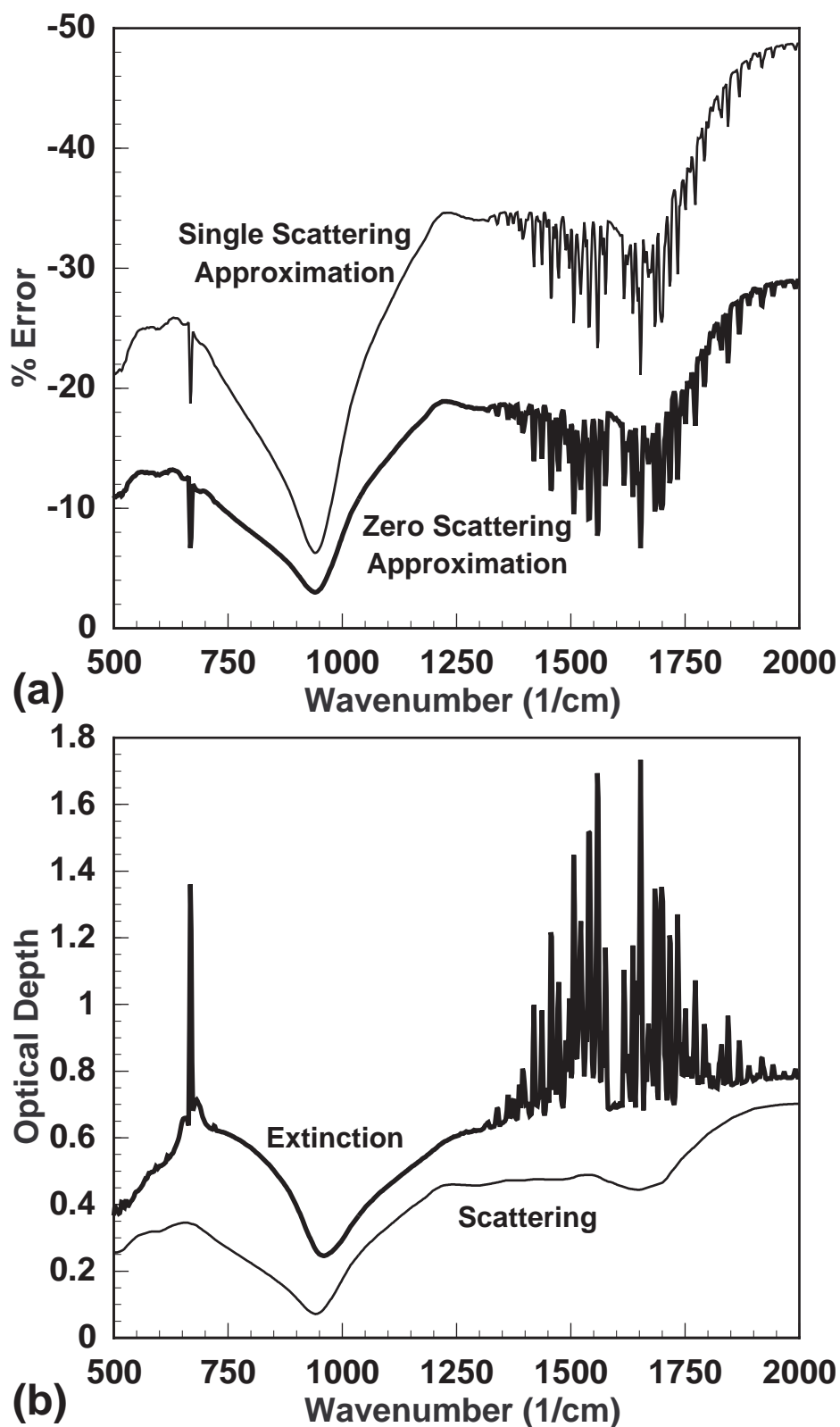


Figure 18.

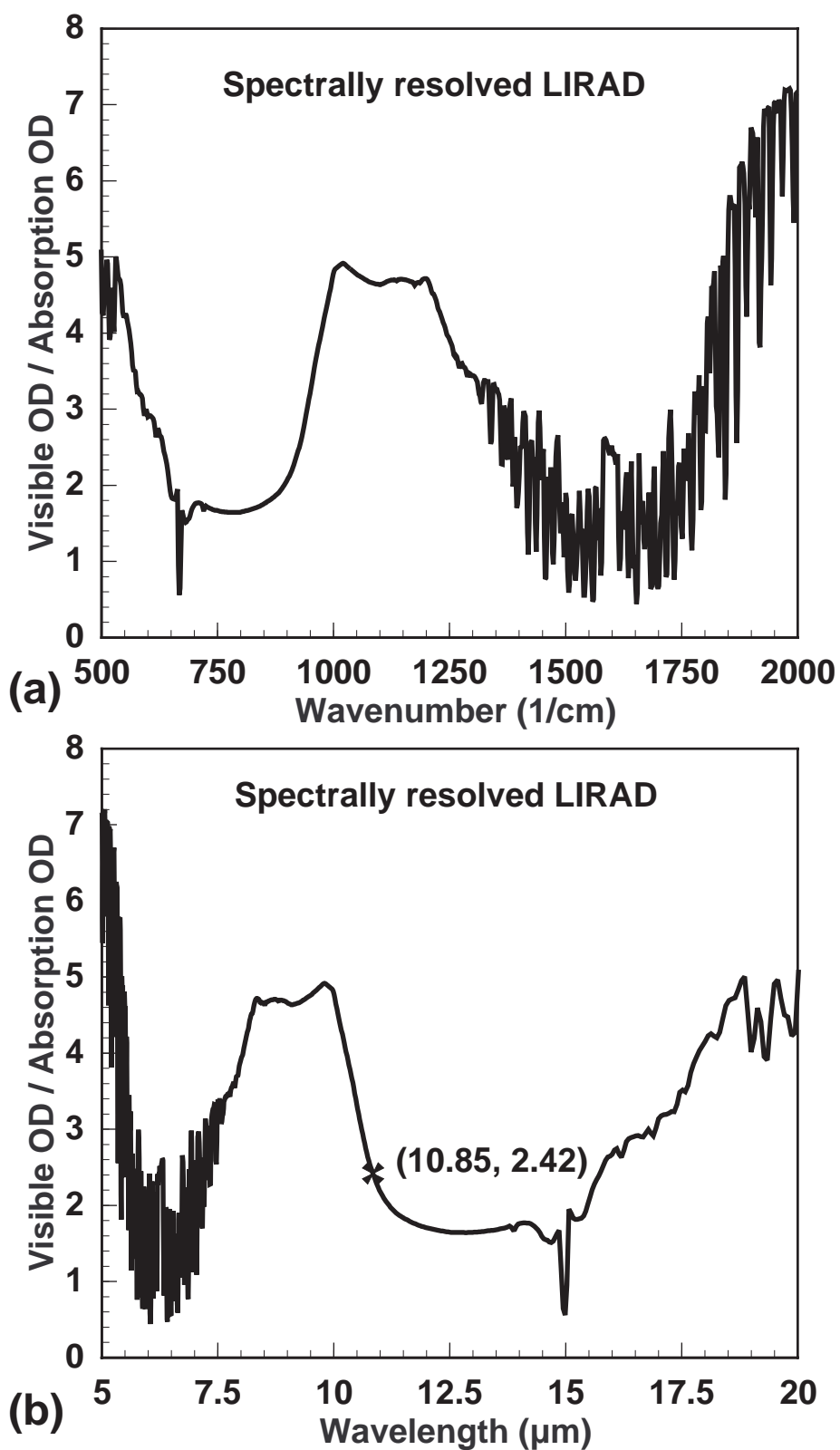


Figure 19.